

GuidedNet: A General CNN Fusion Framework via High-Resolution Guidance for Hyperspectral Image Super-Resolution

Ran Ran¹, Liang-Jian Deng¹, *Member, IEEE*, Tai-Xiang Jiang², *Member, IEEE*, Jin-Fan Hu¹,
 Jocelyn Chanussot³, *Fellow, IEEE*, and Gemine Vivone⁴, *Senior Member, IEEE*

Abstract—Hyperspectral image super-resolution (HSR) is about fusing a low-resolution hyperspectral image (LR-HSI) and a high-resolution multispectral image (HR-MSI) to generate a high-resolution hyperspectral image (HR-HSI). Recently, convolutional neural network (CNN)-based techniques have been extensively investigated for HSR yielding competitive outcomes. However, existing CNN-based methods often require a huge amount of network parameters leading to a heavy computational burden, thus, limiting the generalization ability. In this article, we fully consider the characteristic of the HSR, proposing a general CNN fusion framework with high-resolution guidance, called GuidedNet. This framework consists of two branches, including 1) the high-resolution guidance branch (HGB) that can decompose the high-resolution guidance image into several scales and 2) the feature reconstruction branch (FRB) that takes the low-resolution image and the multiscaled high-resolution guidance images from the HGB to reconstruct the high-resolution fused image. GuidedNet can effectively predict the high-resolution residual details that are added to the upsampled HSI to simultaneously improve spatial quality and preserve spectral information. The proposed framework is implemented using recursive and progressive strategies, which can promote high performance with a significant network parameter reduction, even ensuring network stability by supervising several

intermediate outputs. Additionally, the proposed approach is also suitable for other resolution enhancement tasks, such as remote sensing pansharpening and single-image super-resolution (SISR). Extensive experiments on simulated and real datasets demonstrate that the proposed framework generates state-of-the-art outcomes for several applications (i.e., HSR, pansharpening, and SISR). Finally, an ablation study and more discussions assessing, for example, the network generalization, the low computational cost, and the fewer network parameters, are provided to the readers. The code link is: <https://github.com/Evangelion09/GuidedNet>.

Index Terms—Convolutional neural network (CNN), high-resolution guidance, hyperspectral image super-resolution (HSR), image fusion, pansharpening, single-image super-resolution (SISR).

I. INTRODUCTION

RECENTLY, hyperspectral image super-resolution (HSR), as shown in Fig. 1, has become a fundamental issue in computer vision since it can significantly improve the spatial resolution of low-resolution hyperspectral image (LR-HSI) and the spectral information of high-resolution multispectral image (HR-MSI) to finally yield a fused hyperspectral image (HSI) with both high spatial and spectral resolutions. Many applications can benefit from the fused HSR image, for example, several remote sensing data analysis [1], environment detection [2], classification [3], and recognition [4].

In general, HSR approaches could be roughly classified into two categories. Namely, variational optimization (VO) approaches and deep learning (DL) approaches. The approach proposed in this work falls within the latter class.

VO-based methods are mainly about formulating an optimization model by considering proper regularizers and fidelity terms to solve computer vision problems [7], [8], [9], [10], [11], [12], [13], [14], [15], thus, accurately representing the main properties of the HSR issue at hand [5], [16], [17], [18], [19], [20], [21], [22]. Afterward, some practical algorithms are designed for efficiently solving the given model, estimating the final super-resolved images. Although these VO-based methods produced satisfactory SR results, they need prior information before reconstructing the high-resolution HSI. This information is usually scene dependent, requiring a fine adjustment to be adapted to different real scenarios. Moreover, the computational burden for this class is usually heavy.

Manuscript received 15 March 2022; revised 29 July 2022 and 6 December 2022; accepted 21 December 2022. Date of publication 2 February 2023; date of current version 16 June 2023. This work was supported in part by NSFC under Grant 12271083, Grant 62203089, and Grant 12001446; in part by the Natural Science Foundation of Sichuan Province under Grant 2022NSFSC0501, Grant 2022NSFSC0507, and Grant 2022NSFSC1798; in part by the Key Projects of Applied Basic Research in Sichuan Province under Grant 2020YJ0216; and in part by the National Key Research and Development Program of China under Grant 2020YFA0714001. This article was recommended by Associate Editor Q. M. J. Wu. (*Corresponding author: Liang-Jian Deng.*)

Ran Ran, Liang-Jian Deng, and Jin-Fan Hu are with the School of Mathematical Sciences, University of Electronic Science and Technology of China, Chengdu 611731, Sichuan, China (e-mail: ranran@std.uestc.edu.cn; liangjian.deng@uestc.edu.cn; hujf0206@163.com).

Tai-Xiang Jiang is with the FinTech Innovation Center, Financial Intelligence and Financial Engineering Research Key Laboratory of Sichuan Province, School of Economic Information Engineering, Southwestern University of Finance and Economics, Chengdu 610074, Sichuan, China (e-mail: taixiangjiang@gmail.com).

Jocelyn Chanussot is with the Aerospace Information Research Institute, Chinese Academy of Sciences, Beijing 100045, China, and also with Univ. Grenoble Alpes, Inria, CNRS, Grenoble INP, LJK, 38000 Grenoble, France (e-mail: jocelyn.chanussot@grenoble-inp.fr).

Gemine Vivone is with the National Research Council-Institute of Methodologies for Environmental Analysis, CNR-IMAA, 85050 Tito Scalo, Italy (e-mail: gemine.vivone@imaa.cnr.it).

Color versions of one or more figures in this article are available at <https://doi.org/10.1109/TCYB.2023.3238200>.

Digital Object Identifier 10.1109/TCYB.2023.3238200

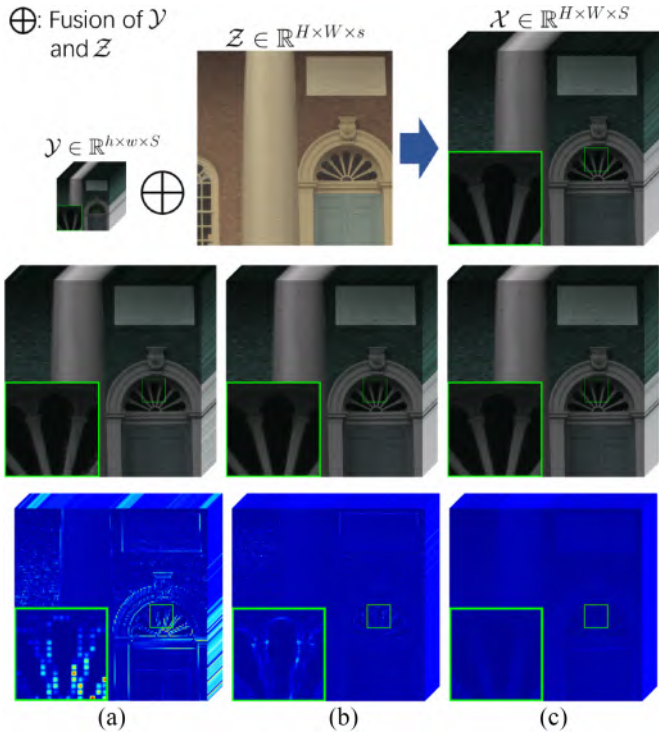


Fig. 1. First row: the schematic of HISR. The image on the right is the HR-HSI \mathcal{X} (i.e., the GT). Second row: the visual results ($8\times$ scale) of (a) subspace-based LTM approach [5] (PSNR = 41.88 dB), (b) MS/HS fusion net (MHF-net) [6] (PSNR = 43.36 dB), and (c) proposed GuidedNet (PSNR = 44.75 dB). Note that all the images are displayed with a pseudo-color RGB format using R = 17th band, G = 30th band, and B = 27th band. Third row: the related error maps. From a visual point of view, our GuidedNet result is the closest to the GT.

In the last decade, DL-based algorithms have been considered to solve several image processing tasks, such as super-resolution [23], [24], [25], [26], image classification [27], and visual question answering [28]. Mainly, convolutional neural network (CNN), as core technique of DL-based approaches, has been applied to HISR [29], [30], [31], [32], [33], [34], [35], [36], [37], getting promising results. These DL methods can learn the relationship between the HSI and the ground truth (GT). They showed satisfactory performance in the HISR task. However, these methods still have some drawbacks. First, some methods have a complex network structure and a considerable amount of network parameters to severely consume computing resources taking a long time for training and execution. Second, previous methods generally utilize the entire MSI without extracting multiscale spatial features. The high-resolution HSI's (HR-HSI) features significantly differ from LR-HSI's features leading to obstructions in fusion and reconstruction on a large scale. Third, some DL-based methods cannot easily extend to other image SR problems (e.g., pansharpening, or SISR) with satisfying results. Hence, the above-mentioned issues motivate us to further improve DL-based HISR approaches.

In this article, we propose the so-called GuidedNet introducing two crucial branches (mainly for the application to HISR). The first one is the high-resolution guidance branch (HGB) decomposing an image into several scales that are fully exploited into the subsequent fusion branch. The other is the

feature reconstruction branch (FRB), which can fuse the LR input and the multiscale information from the HGB to produce the final HR output. Besides, recursive blocks are also integrated into the proposed network architecture, leading to fewer network parameters and less computational time while maintaining high-quality outcomes.

In summary, the main contributions are as follows.

- 1) A general CNN fusion framework is proposed in this article. We successfully applied it to multiple image resolution enhancement problems, such as HISR, pansharpening, and SISR, in the meanwhile obtaining state-of-the-art (SOTA) performance for each task.
- 2) Two novel network branches, that is, the FRB and the HGB, are designed to utilize multiscale information of high-resolution guidance images and reconstruct the fused high-resolution output. In particular, the two developed branches have the following characteristics, that is, multiscale information fusion, progressive feature injection, and gradual feature reconstruction. Rich structural information can be captured more accurately by using a receptive field from wide to fine in a multiscale framework. Compared with direct upsampling, which leads to difficulties in learning mapping functions and blur effects for large scaling factors, a progressive structure can better address the problem by adapting it to large-scale super-resolution. Moreover, intermediate results predicted by GuidedNet are supervised, aiding network stability. Thanks to these characteristics, GuidedNet can easily obtain promising outcomes for resolution enhancement.
- 3) GuidedNet has several advantages with respect to previously developed approaches: SOTA performance thanks to the designed network architecture, fewer network parameters thanks to the usage of recursive blocks, a remarkable ability to upsample to several scales, and good adaptability to other image resolution enhancement tasks (verified in the experimental section).

The organization of this article is as follows. Section II will briefly introduce the related works. In Section III, we will describe the proposed network architecture, including the two designed network branches, the recursive blocks, and the training details. In Section IV, we conduct extensive experiments to assess the effectiveness of the proposed network for HISR. Finally, conclusions are drawn in Section V.

II. RELATED WORKS

A. Related Works

In general, the relationship between the HR-HSI, the LR-HSI, and the HR-MSI can be expressed by the following linear models [38]:

$$\begin{aligned} \mathbf{Y} &= \mathbf{XBS} + \mathbf{N}_Y \\ \mathbf{Z} &= \mathbf{RX} + \mathbf{N}_Z \end{aligned} \quad (1)$$

where $\mathbf{Z} \in \mathbb{R}^{HW \times s}$, $\mathbf{Y} \in \mathbb{R}^{hw \times S}$, and $\mathbf{X} \in \mathbb{R}^{HW \times S}$ represent the input HR-MSI, LR-HSI, and the target HR-HSI, respectively. H and W are the height and width of the target resolution, that is, the height and width of HR-MSI and HR-HSI, and

h and w are the height and width of the input LR-HSI. S is the number of spectral bands of the HSI, and s is the number of spectral bands of the LR-MSI. $\mathbf{B} \in \mathbb{R}^{HW \times HW}$ represents the circular convolution operator, $\mathbf{S} \in \mathbb{R}^{HW \times hw}$ represents the downsampling operator, and $\mathbf{R} \in \mathbb{R}^{s \times S}$ is the spectral response matrix of the HR-MSI. \mathbf{N}_Y and \mathbf{N}_Z are the noises related to the LR-HSI and the HR-MSI, respectively.

Based on the above models, many studies have been proposed with effective solutions for the HSI super-resolution problem (see [5], [17], [18], [19], [39]). For instance, in [17], spectral unmixing and sparse coding ideas have been studied to enhance the resolution of HSIs. Yokoya et al. [18] developed a coupled non-negative matrix factorization (CNMF) unmixing algorithm using a linear spectral mixture model, which can effectively and efficiently obtain competitive HISR results. Dian et al. [19] clustered the HR-MSI and the HR-HSI, respectively, applying a low-tensor-train rank (LTTR) constraint to transform the HISR into an optimization problem, thus, achieving excellent outcomes. Dian et al. [21] exploited a CNN denoiser to regularize the fusion procedure, achieving excellent fusion performance without needing additional HSIs and MSIs for the pretraining stage.

However, since it is generally necessary to assume some subjective priors, traditional methods are sensitive to the change of scenario showing difficulties when applied to different scenes. Recently, DL methods based on CNNs have been widely exploited for various low-level vision tasks [23], [40], [41], [42]. For example, Lim et al. designed EDSR [40] using residual networks and achieved competitive single-image super-resolution (SISR) outcomes. Zeng et al. [41] learned the intrinsic representations of LR and HR image blocks via a proposed coupled deep autoencoder (CDA) holding outstanding performance for SISR. CNN-based methods, for example, [6], [29], [30], and [37], can solve the HISR problem without relying upon subjective priors. Dian et al. [29] proposed a novel deep CNN-based HSI and MSI fusion method, which considers the imaging model of the HSI and MSI and achieves superior fusion performance. Palsson et al. [30] proposed a 3-D CNN network using a principal component analysis to fuse HR-MSI and LR-HSI. This method significantly reduces the computational cost and has stronger robustness to noise. Zhu et al. [33] proposed a lightweight progressive zero-centric residual network. Xie et al. designed an HISR model according to [31, eq. (1)], then constructed the solving algorithm using the approximate gradient method. After that, a new fusion network, called MHF-net [6], is designed by expanding this solving algorithm. Benefiting from excellent preservation of the spectral and spatial details, the MHF-net outperforms other DL-based approaches, currently representing a SOTA HISR method.

HISR is closely related to the multispectral image pansharpening task. In this work, we also extend our method to the pansharpening task. The pansharpening problem reconstructs the HR-MSI by fusing an LR-MSI and an HR panchromatic (PAN) image. Traditional pansharpening approaches are represented by both component substitution (CS) and multiresolution analysis (MRA)-based methods. CS-based methods, such as the band dependent on spatial detail (BDS) [43]

and the BDS with physical constraints (BDS-PCs) [44], can produce acceptable spatial fidelity outcomes but introduce spectral distortion. The class of MRA-based methods contains the generalized Laplacian pyramid (GLP) [45] and the GLP at full resolution for regression-based (GLP-Reg) [46].

Many DL-based methods have been designed for the pansharpening problem yielding competitive performance (see [47], [48], [49], [50], [51], [52], [53]). Masi et al. [48] adapted a simple three-layer convolution network for pansharpening. Yang et al. [47] proposed a deep network structure (PanNet) that focuses on spectral and spatial preservation by training the network in the high-pass domain through a high-pass filter. Deng et al. [52] combined the traditional CS and MRA fusion schemes developing a deep network (FusionNet) that extracts high-quality details, achieving competitive performance. However, pansharpening reaching high spatial resolutions can generate significant spectral distortion. The introduction and the full use of progressive and multiscale architectures in pansharpening can alleviate this issue.

In what follows, we will present the proposed general fusion framework in more detail.

III. PROPOSED GUIDEDNET

In this section, we present the motivation under the developing of the proposed method, the designed network, including the network architecture consisting of the two proposed branches, the recursive mechanism for parameter reduction, the loss function for multiscale training, and some network training details.

A. Motivation

Some above-mentioned issues, such as progressive feature injection, gradual feature reconstruction, and parameter sharing, have motivated us to develop a general CNN fusion framework, which can fully consider, in a simple manner, a progressive multiscale structure (PMS) for the HISR problem. Besides, we also expect to achieve promising outcomes with a significant network parameters reduction. Meanwhile, we hope that the proposed architecture can easily be extended to multiple image fusion tasks promoting the design of a general fusion framework. Thus, we need to design two branches for the two inputs of the fusion task, guaranteeing sufficient information exchange and communication from the different inputs. In addition, spatial information is fused into the feature domain. Therefore, in the reconstruction branch, the network has a dual data stream (DDS) coming from the feature and the image domains, which are connected through a residual learning module.

B. Overall Network Architecture

This work aims to formulate a general fusion framework for image fusion tasks while fully exploiting multiscale information, progressive feature injection, and gradual feature reconstruction. To reach this goal, we design a general CNN fusion framework via high-resolution guidance for image fusion, that is, the proposed GuidedNet. The overall and

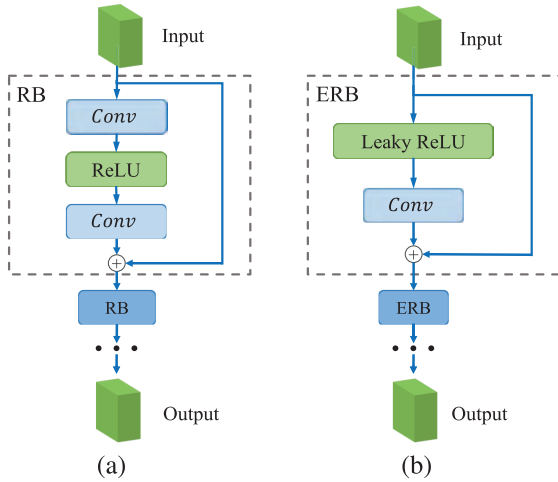


Fig. 4. (a) Structure of the conventional ResNet with the RB. (b) Structure of the ResNet with the ERB (ResNet-ERB), which is used in the GuidedNet.

for the depth map super-resolution in [55], GuidedNet shows several differences in the fusion mode exploiting a gradual feature reconstruction (see Section III-B3 for details).

The generation of the multiscale high-resolution guidance image can be expressed as follows:

$$\mathcal{Z}_k = \text{Downsample}(\mathcal{Z}_{k+1}, \Theta_d) \quad (2)$$

where Downsample represents the downsampling network consisting of 2-D convolutions, Θ_d indicates the network parameters to be trained, \mathcal{Z}_k is the guidance image of size $2^k h \times 2^k w \times s$ at the k th stage of the HGB with $k = 1, 2, \dots, n-1$, and n is the total number of layers.

2) *Feature Reconstruction Branch*: The FRB is about progressively injecting the high-frequency details from the high-resolution input (i.e., the HR-MSI) on different scales into the LR-HSI (see the bottom side in Fig. 2).

a) *FRB flow*: The LR-HSI feature \mathcal{F}_0 is extracted first through a convolutional layer Conv_1 with parameters indicated as Θ_1

$$\mathcal{F}_0 = \text{Conv}_1(\mathcal{Y}, \Theta_1) \quad (3)$$

then the extracted LR-HSI feature is considered by the designed DFM to complete the spatial feature reconstruction by incorporating the high-resolution input on the smallest scale (i.e., \mathcal{Z}_1). The reconstructed HR-HSI comes from the previous level.¹ The details about DFM can be found in Section III-B2. When the fusion procedure by the recursive DFM is ended, we obtain two outputs, that is, the reconstructed HR-HSI feature \mathcal{F}_1 and the HR-HSI image $\hat{\mathcal{X}}_1$ at a finer scale. Afterward, the two obtained outputs and the high-resolution input at a finer scale are considered in the next DFM. This structure of two data in parallel is called DDS, and after repeating this process several times, the final HR-HSI is yielded by the FRB.

b) *DFM*: This section is devoted to presenting the DFM. This module incorporates three inputs (i.e., the high-resolution input from the HGB, the reconstructed HR-HSI feature, and

¹Note that the reconstructed HR-HSI for the starting (first) level is the LR-HSI, that is, \mathcal{Y} .

the HR-HSI image from the previous step) into a designed convolutional module for gradually injecting high-frequency information into the HSI. This module considers first a feature upsampling consisting of a convolution operation and a deconvolution strategy to increase the feature size at a finer scale (corresponding to the scale of the high-resolution input provided by the HGB). Then, the upsampled HSI feature is concatenated with the high-resolution guidance from the HGB, seen as a new feature with detailed information. The number of channels of the new feature is restored by a simple convolutional layer

$$\hat{\mathcal{F}}_k = \text{Conv}_f(\text{Upsample}(\mathcal{F}_{k-1}), \mathcal{Z}_k, \Theta_f) \quad (4)$$

where $\hat{\mathcal{F}}_k$ represents a feature with size $2^k h \times 2^k w \times C$, $\hat{\mathcal{F}}_{k-1}$ is another feature with size $2^{k-1} h \times 2^{k-1} w \times C$, \mathcal{Z}_k is the high-resolution guidance from the HGB, and Θ_f indicates the parameters to be trained.

A unique ResNet accounting for efficient residual blocks (ERBs), called ResNet-ERB, is designed to fuse details and reconstruct high-resolution HSI features. Generally, the ResNet consists of two convolution layers and an activation function in the middle, as shown in Fig. 4(a). However, as the depth of the ResNet increases, the gradient information tends to vanish when it reaches the end because of a significant amount of redundancy in the deep ResNet [56]. Too many convolutions with limited benefits can increase the computational burden, thus, suggesting the simplification of the network by removing the superfluous layers. For image spatial enhancement tasks, feature propagation can be strengthened by creating short paths from early to later layers. Therefore, the proposed DFM utilizes a ResNet, including an ERB. In the proposed ERB, just a LeakyReLU activation function and a convolutional layer are adopted to simplify the network structure, improving efficiency. The structure is shown in Fig. 4(b); several blocks are connected in a row to form the final ResNet-ERB module. Thus, the network reduces the number of parameters thanks to the more straightforward structure of the block. Furthermore, this block structure can extract features more effectively, reducing the difficulty of the network in the learning phase (preventing gradient exploding). ResNet-ERB is represented in our network as

$$\mathcal{F}_k = \text{ResNet}_{\text{ERB}}(\hat{\mathcal{F}}_k, \Theta_e) \quad (5)$$

where $\text{ResNet}_{\text{ERB}}$ is the ResNet-ERB function, \mathcal{F}_k is the output feature, and Θ_e is the set of parameters to be learned.

Through this design, the spatial details of the guidances are gradually injected into the HSI features in the DFM related to the different layers. Fig. 5 shows a visual comparison of the features \mathcal{F}_k ($k \in \{1, 2, 3\}$) of the DFM for the different layers. Specifically, in the *chart and stuffed toy* test case from the CAVE dataset, we selected the 31st, the 54th, and the 15th bands of the feature maps as R, G, and B, respectively, and the images are sampled to reach the same size for visualization purposes. The figure shows that the spatial detail information in the three features increases.

After generating the reconstructed high-resolution features as the output of the ResNet-ERB, the residual image is predicted by a residual reconstruction module consisting of a

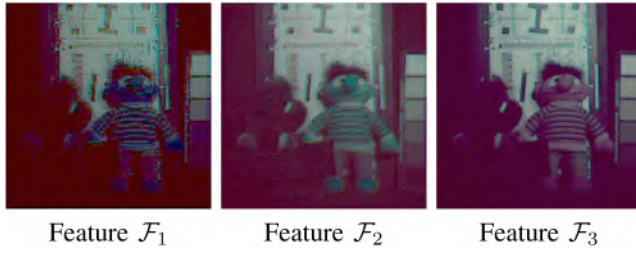


Fig. 5. Visual comparison of \mathcal{F}_1 , \mathcal{F}_2 , and \mathcal{F}_3 extracted from the first DFM, the second DFM, and the third DFM, respectively. Note that the images are scaled to the same size for a better visualization.

convolutional layer to adjust channels. In the other stream, the LR-HSI is upsampled with a factor of 2 by an upsampling block, that is, the pixel shuffle (PS) (called subpixel convolution).² The operation is shown in Fig. 3(a). Finally, the upsampled image is added to the residual image to reconstruct the final HR-HSI. Thus, we have

$$\mathcal{X}_k^U = \text{PS}(\tilde{\mathcal{X}}_{k-1}, \Theta_p) \quad (6)$$

where PS is the pixel shuffle function providing the upsampling of the input data, \mathcal{X}_k^U is the upsampled image at the k th level, and Θ_p indicates the set of parameters to be trained

$$\tilde{\mathcal{X}}_k = \text{resRecon}(\mathcal{F}_k, \Theta_r) + \mathcal{X}_k^U \quad (7)$$

$\text{resRecon}(\cdot)$ represents the residual reconstruction module to predict a residual image from \mathcal{F}_k , and Θ_r indicates the set of parameters. It is worth to be remarked that if $k = 1$, $\tilde{\mathcal{X}}_{k-1}$ is equal to \mathcal{Y} .

c) *Recursive mechanism for DFMs*: After determining the DFM, the GuidedNet approach repeats the DFM several times to reach the desired resolution of the HSI. Since the DFMs for different scales hold the same network structure, we can use the recursive mechanism for each DFM to significantly reduce the network parameters. Besides, thanks to the repetitive usage of the DFM, the proposed network can theoretically get fusion outcomes with any scaling factor power of 2. For example, we tested the performance of our GuidedNet considering the HISR application with scaling factors of 4, 8, 16, and 32 (see Section III-B2).

3) *Comparison With Previous Works*: The GuidedNet is related to previous works, such as the BDPN [54] and the MSGNet [55], which use different resolutions for bidirectional multiscale feature enhancement. Compared with the BDPN, the GuidedNet strongly focuses on fusing features into two branches to extract details, while BDPN just uses a simple addition operator to solve this problem. The guidance images must be mapped into the feature space when fusing the low-resolution image. Hence, we attach importance in the GuidedNet to the mapping learning among image features. Compared with the MSGNet, the GuidedNet generates intermediate results many times and adopts multiscale loss training to ensure spectral preservation and stability. In addition, the fusion step for the MSGNet approach is just based on a simple convolution, reducing the task's efficiency. Finally,

²The PS approach expands, by a convolutional layer, the LR-HSI with size $h \times w \times S$ to reach the size of $rh \times rw \times S$, where r is the scaling factor.

the GuidedNet achieves multiscale fusion and reconstruction into the feature domain, and thanks to its sharing strategy, it can significantly reduce the network parameters.

C. Loss Function

In the GuidedNet, several intermediate outputs, that is, $\tilde{\mathcal{X}}_i$, $i = 1, 2, \dots, L$, are generated by the recursive DFMs. These outputs can progressively generate the final HR output with the desired scale through the specially designed network architecture. For a better supervision of the network learning, it is better to enforce a mean-square error (MSE) loss between the output of a given scale and the corresponding downsampled GT image. Thus, the final loss function is a multiple-loss one, which is defined as follows:

$$\begin{aligned} \mathcal{L}(\mathcal{Y}, \mathcal{Z}_n, \mathcal{X}_n; \Theta) &= \sum_{k \in K} \alpha_k \mathcal{L}_k(\mathcal{Y}, \mathcal{Z}_k, \mathcal{X}_k; \Theta) \\ \mathcal{L}_k(\mathcal{Y}, \mathcal{Z}_k, \mathcal{X}_k; \Theta) &= \left\| \tilde{\mathcal{X}}_k - \mathcal{X}_k \right\|_F^2 \end{aligned} \quad (8)$$

where k represents the layer number of the reconstructed HSI, Θ involves all the related network parameters to be learned, \mathcal{Y} and \mathcal{Z}_n are the LR-HSI and the maximum resolution guidance image in input, respectively, \mathcal{X}_k represents the HR-HSI at the k th layer, K indicates all the layer numbers (with $K = \{1, 2, \dots, n\}$), and α_k is the weight of each subloss function at the k th layer.

The weights can be set in several ways. An attempt is to set them considering the approximation degree to the final result, that is, the weight gradually becomes more significant as the scale increases. For instance, if the SR ratio is 8, we set $K = \{1, 2, 3\}$, and α_1 , α_2 , and α_3 are set to 1, 2, and 4, respectively. However, the network's stability could be reduced, and the prediction results could appear highly distorted under this setting. This is because the intermediate results are not significantly supervised. Another possibility is to increase the weights of the intermediate results to solve this problem. Thus, α_1 , α_2 , and α_3 can be set to 4, 2, and 1, respectively, to improve stability and accuracy. Indeed, the network architecture is trained progressively. Thus, if we take larger weights for the initial and intermediate loss functions (i.e., layers 1 and 2), we can have a better final HR image reconstruction, even if we use a smaller weight for the final layer (i.e., layer 3) (see also the ablation study in Section IV-C).

D. Network Training Details

1) *Network Details*: This section is devoted to showing more network details. More specifically, the number of channels C for all the features is set to 64, the sizes of all the convolutional kernels are 3×3 , the sizes of all the down-sampling convolution and deconvolution kernels are 6×6 , and the padding type of all the convolutions is set as "SAME." Additionally, all the related activation functions use the LeakyReLU with a slope of 0.2 when $x < 0$. In particular, the number of ERBs for a scale in the ResNet-ERB is 10, and the ERB structure is shown in Fig. 4(b).

2) *Training Data*: We use the CAVE dataset [60] to train and test all the compared methods. This dataset consists of

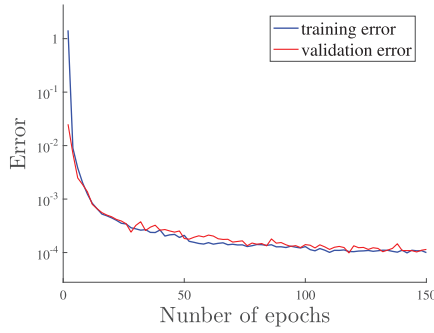


Fig. 6. Training and validation errors of our GuidedNet.

32 HSIs with a size of $512 \times 512 \times 31$ and corresponding RGB images with a size of $512 \times 512 \times 3$ (viewed as multispectral images, MSIs), which are generated by a general spectral response function \mathbf{R} to simulate the Nikon D700 camera. This dataset has also been used in [5], [19], and [31]. We selected 21 HSIs as the training set and 11 HSIs as the testing set. To reduce the storage cost, we crop the original HSIs (HR-HSIs) and MSIs (HR-MSIs) into sizes of $80 \times 80 \times 31$ and $80 \times 80 \times 3$, respectively. Then, we simulate LR-HSIs ($10 \times 10 \times 31$, scale = 8) by adopting a Gaussian blur with a kernel of 3×3 and a standard deviation of 0.5 to HR-HSIs and taking $8 \times$ bicubic downsampling. Moreover, the involved intermediate GT HSIs (GT-HSIs), $\tilde{\mathcal{X}}$, are also obtained by bicubic downsampling. Note that all the simulated LR-HSIs, HR-MSIs, HR-HSIs, and GT-HSIs from the 21 samples are divided into two parts: 1) training set (90%) and 2) validation set (10%).

Similar to the CAVE dataset, the Harvard dataset [61] consists of 77 HSIs in indoor and outdoor scenes with a spatial resolution of 1024×1392 and 31 spectral bands with a size of $1024 \times 1392 \times 31$. We selected 20 images as the training set. Moreover, we randomly selected ten HSIs from the Harvard dataset cutting the upper left 1000×1000 side of the image as the testing set. The data simulation process is the same as that of the CAVE dataset.

3) *Training Details*: For fairness, all the DL-based approaches are implemented and trained in Tensorflow 1.8 framework on an NVIDIA GeForce GTX 2080Ti (11G RAM) and 2.90-GHz Intel i5-9400F (32G Memory). The Adam optimizer [62] trained our GuidedNet with a learning rate of 0.00001. Furthermore, the training epochs are set to 150, and the mini-batch size is 32. Fig. 6 plots the errors of the proposed GuidedNet on the training and validation datasets at each epoch separately, demonstrating its good convergence. For the other compared DL methods (e.g., the MHF-net and HSRnet), we consider the available source codes for both training and testing, thus, ensuring a fair comparison.

IV. EXPERIMENTS

This section analyzes first the qualitative and quantitative performance of HISR. Then, extensive discussions on the super-resolution ability of the proposed GuidedNet are provided to the readers. After that, we extend the given method to a remote sensing fusion task, that is, the multispectral pansharpening. Finally, we show that the proposed

TABLE I
AVERAGE QUALITY INDICES WITH RELATED STANDARD DEVIATIONS OF THE RESULTS PROVIDED BY ALL THE COMPARED METHODS ON 11 TESTING IMAGES FROM THE CAVE DATASET. THE BEST RESULTS ARE HIGHLIGHTED

Method	PSNR	SAM	ERGAS	SSIM
CNMF [18]	32.97±2.6	10.98±3.8	4.27±2.9	0.909±0.04
FUSE [57]	29.21±2.4	23.04±10.2	6.04±4.5	0.791±0.08
GLP-HS [58]	32.25±2.2	10.15±3.6	3.99±2.2	0.916±0.03
LTTR [19]	37.56±2.8	5.35±1.9	2.21±1.0	0.970±0.02
LTMR [5]	37.56±2.7	5.36±1.8	2.15±1.0	0.970±0.02
IR-TenSR [59]	37.58±2.7	7.44±2.7	2.12±0.9	0.959±0.02
MHF-net [6]	45.00±3.1	4.88±1.9	0.99±0.7	0.989±0.01
HSRnet [37]	44.88±3.5	3.74±1.4	0.98±0.6	0.991±0.00
GuidedNet	45.41±3.6	4.03±1.4	0.97±0.7	0.991±0.00

network architecture can be viewed as a general framework that can enhance spatial resolution only if there is a high-resolution branch as guidance. Thus, the given framework is also extended to another super-resolution problem, that is, the SISR, adding HR guidance.

More in detail, we assess the performance of the proposed network by exploiting several SOTA HISR methods, such as the fusion using CNMF unmixing [18], the fast fusion based on Sylvester equation (FUSE) approach [57], the GLP approach for hypersharpening (GLP-HS) [58], the LTTR-based approach [19], the subspace-based low-tensor multirank regularization (LTMR) approach [5], the iterative regularization based on tensor subspace representation (IR-TenSR) [59], the MS/HS fusion network (MHF-net) [6], and the HSRnet [37], on the CAVE dataset [60] and the Harvard dataset [61]. Four widely used quality indexes (QIs) for HISR are utilized to evaluate the performance quantitatively, that is, the peak signal-to-noise ratio (PSNR), the spectral angle mapper (SAM [63]), and the erreur relative globale adimensionnelle de synthèse (ERGAS [64]), and the structure similarity (SSIM [65]). The higher the values of the PSNR and the SSIM, the better the performance. Conversely, the smaller the values of the SAM and the ERGAS, the better the performance. For a fair comparison, all the compared methods are tested on the same GPU or CPU (see the training details in Section III-D).

A. Experiments on CAVE Dataset

We conduct simulated experiments on the CAVE image dataset to verify the effectiveness of the proposed GuidedNet. We generate the HR-MSI by combining all the GT-HSI bands according to the spectral response function, \mathbf{R} . Then, we simulate the LR-HSI by downsampling the GT-HSI with a factor of 8. This process is described in Section IV-B. The testing dataset is formed by 11 HSIs from the CAVE dataset with a size of $512 \times 512 \times 31$.

The average QIs and the corresponding standard deviations, calculated on all the testing data, are shown in Table I. Table II reports the QIs for some specific test cases, that is, the *chart and stuffed toy* and the *fake and real tomatoes*, and the average running times on all the testing data. These tables clearly show that the GuidedNet outperforms the other methods, even requiring less computational burden. In Fig. 7,

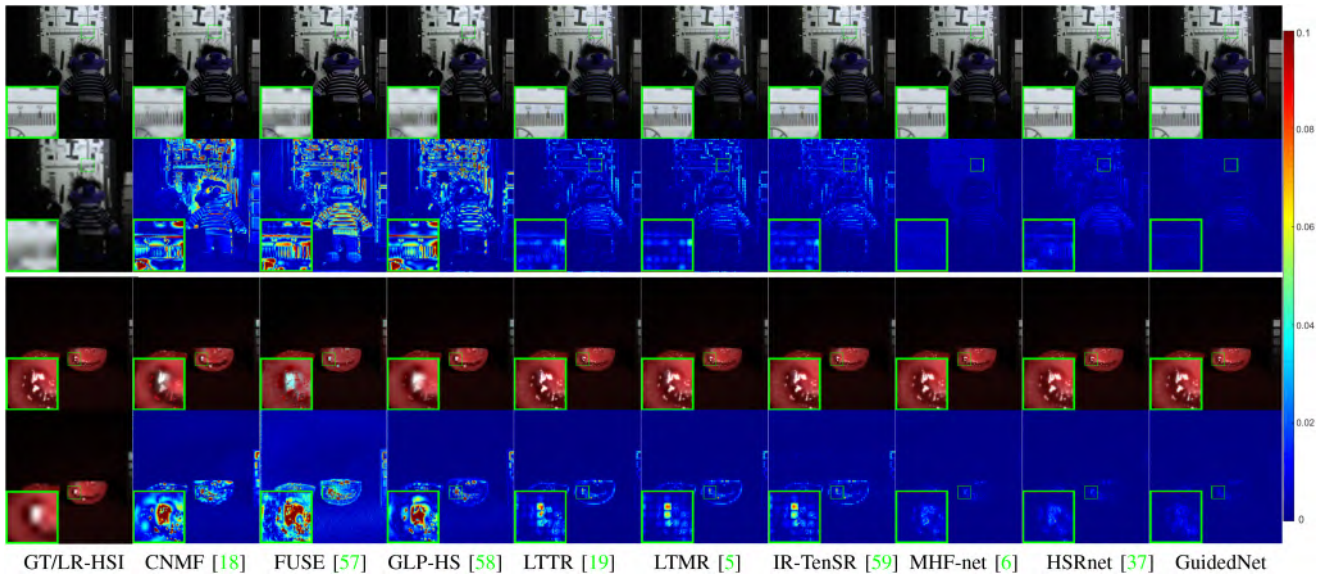


Fig. 7. First column: the GTs and the corresponding LR-HSI images (in pseudo-colors) for the *chart and stuffed toy* (R-16, G-15, B-21) (1st and 2nd rows) and the *fake and real tomatoes* (R-31, G-15, B-16) (3rd and 4th rows) test cases from the CAVE dataset. The 2nd–8th columns: the visual results and the related error maps for all the compared approaches. A zoomed area has been added to aid the visual inspection.

TABLE II

QIS VALUES AND THE AVERAGE RUNNING TIMES FOR THE COMPARED METHODS ON TWO TEST CASES FROM THE CAVE DATASET. G MEANS THAT THE METHOD EXPLOITS THE GPU, INSTEAD, C MEANS THAT IT EXPLOITS THE CPU. THE BEST RESULTS ARE HIGHLIGHTED

Method	<i>chart and stuffed toy</i>				<i>fake and real tomatoes</i>				Time s
	PSNR	SAM	ERGAS	SSIM	PSNR	SAM	ERGAS	SSIM	
CNMF	30.35	9.23	2.80	0.936	41.54	6.38	12.68	0.964	14.5(C)
FUSE	29.14	12.53	3.33	0.890	38.65	7.80	8.41	0.967	4.1(C)
GLP-HS	29.52	8.33	3.02	0.930	38.32	6.33	8.21	0.974	5.2(C)
LTTR	35.45	6.03	1.62	0.964	42.50	5.53	3.69	0.987	1543.6(C)
LTMR	35.78	6.47	3.08	0.965	42.33	5.51	6.96	0.987	812.6(C)
IR-TenSR	35.80	6.22	2.94	0.964	42.55	5.60	4.64	0.987	211.9(C)
MHF-net	43.02	5.17	0.72	0.991	48.73	6.79	1.69	0.991	0.75(G)
HSRnet	43.13	4.95	0.74	0.992	48.65	5.07	1.66	0.994	0.31(G)
GuidedNet	44.15	4.19	0.59	0.993	49.70	5.01	1.48	0.995	0.26(G)

to show the visual comparison, we draw some pseudo-color images of the HSI super-resolution results and the corresponding error maps on the *chart and stuffed toy* and the *fake and real tomatoes* test cases, from the CAVE dataset. It can be observed from the error maps that CNMF, FUSE, GLP-HS, LTTR, LTMR, and IR-TenSR introduce artifacts. Conversely, the MHF-net and HSRnet, belonging to the DL class, perform better than the above-mentioned traditional methods but still performing unsatisfactorily on the reproduction of details. Instead, the residual map between our method and the GT image contains fewer errors for the compared approaches, thus, showing a better spatial detail reconstruction. Another analysis is about spectral fidelity. In Fig. 8, to better compare the effects of spectral preservation, we plot the spectral vectors for all the compared approaches on the two mentioned test cases by fixing a pixel to provide this analysis. The spectral vectors generated by the proposed GuidedNet and the GT are very similar, demonstrating the ability of GuidedNet to reduce spectral distortion.

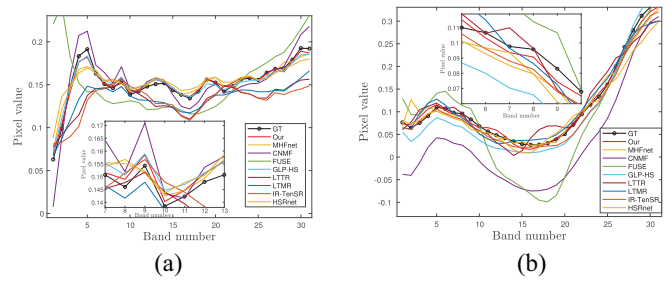


Fig. 8. Spectral vectors analysis of the GT and coming from the outcomes of the compared approaches for the (a) *chart and stuffed toy* located at (251,255) and (b) *fake and real tomatoes* located at (230, 241).

B. Experiments on Harvard Dataset

Table III reports the QIs and the corresponding standard deviations for all the compared methods on the Harvard testing data. We observe that the GuidedNet outperforms all the compared approaches considering the PSNR, SAM, and SSIM as metrics. For the ERGAS metric, GuidedNet ranks second. Again, we show the visual comparison displaying pseudo-color images and the related error maps on two specific test cases (see Fig. 9). The GuidedNet yields better visual results in agreement with the quantitative analysis.

C. Ablation Study

This section is about several ablation studies to assess the effectiveness of the GuidedNet, mainly concerning PS, DFM, and loss function.

1) *Pixel Shuffle*: The GuidedNet employs PS to upsample the LR-HSI to a larger image size. To verify the effectiveness of PS compared with traditional methods, we change the upsampling of the recursive DFMs to deconvolution while keeping the remaining network structure to conduct comparative experiments on both CAVE and Harvard training datasets.

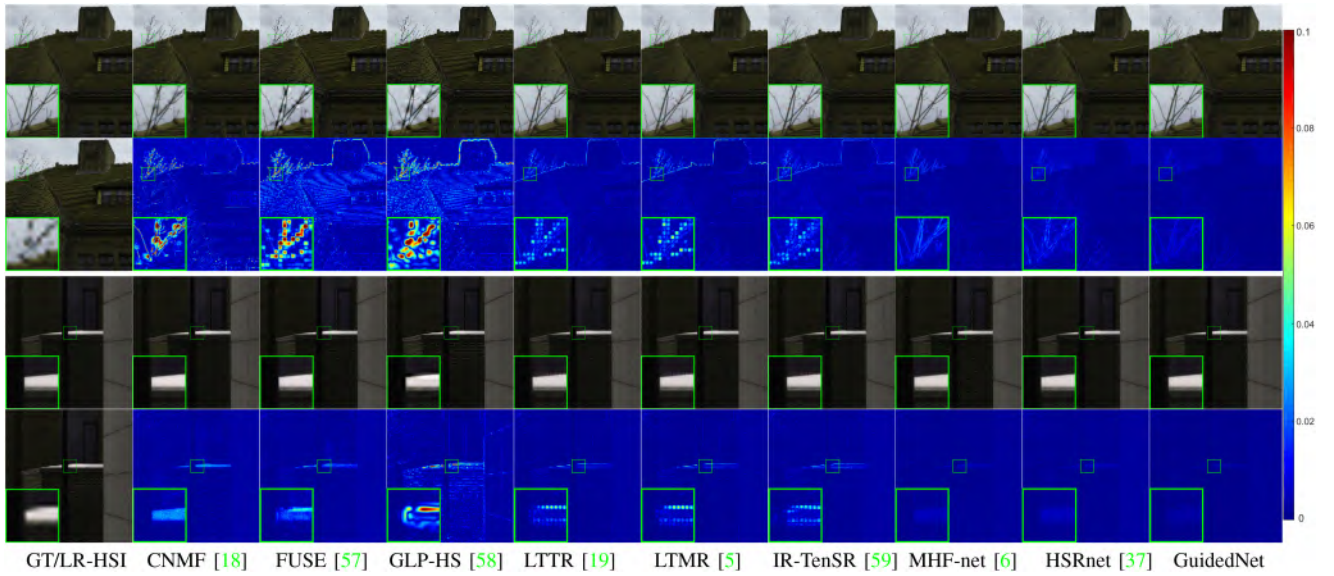


Fig. 9. First column: the GTs and the corresponding LR-HSI images (in pseudo-colors) for the *house* (R-23, G-18, B-14) (1st and 2nd rows) and the *fence* (R-20, G-21, B-13) (3rd and 4th rows) test cases from the Harvard dataset. The 2nd–8th columns: the visual results and the related error maps for all the compared approaches. A zoomed area has been added to aid the visual inspection.

TABLE III

AVERAGE QIS WITH THE RELATED STANDARD DEVIATIONS OF THE RESULTS PROVIDED BY ALL THE COMPARED METHODS ON TEN TESTING IMAGES FROM THE HARVARD DATASET. THE BEST RESULTS ARE HIGHLIGHTED

Method	PSNR	SAM	ERGAS	SSIM
CNMF [18]	39.54±5.0	3.33±1.0	1.71±0.9	0.974±0.02
FUSE [57]	38.04±5.2	4.11±1.5	1.69±0.8	0.969±0.02
GLP-HS [58]	38.97±4.4	3.96±1.3	2.14±0.8	0.960±0.02
LTTR [19]	38.38±5.0	3.81±1.4	2.06±0.8	0.966±0.02
LTMR [5]	39.56±4.4	3.54±1.3	1.66±1.1	0.970±0.02
IR-TenSR [59]	38.84±4.9	3.97±1.5	1.87±0.7	0.966±0.02
MHF-net [6]	41.60±5.9	3.51±1.2	1.29±0.6	0.977±0.02
HSRnet [37]	41.52±6.1	2.96±1.0	1.18±0.4	0.980±0.02
GuidedNet	41.64±6.3	2.85±1.0	1.20±0.5	0.981±0.02

TABLE IV

AVERAGE QIS WITH THE RELATED STANDARD DEVIATIONS OF THE RESULTS PROVIDED BY THE GUIDEDNET APPROACH USING DECONVOLUTION OR PS FOR LR-HSI UPSAMPLING

CAVE				
Method	PSNR	SAM	ERGAS	SSIM
Deconv	44.87±3.6	4.17±1.4	1.01±0.7	0.991±0.01
PS	45.41±3.6	4.03±1.4	0.97±0.7	0.991±0.00
Harvard				
Method	PSNR	SAM	ERGAS	SSIM
Deconv	36.43±7.5	6.03±3.8	3.86±2.9	0.945±0.06
PS	37.96±6.8	4.48±2.0	3.52±2.5	0.961±0.03

The average QIs, shown in Table IV, demonstrate that the current setting is the best choice for the HISR task.

2) *Efficient Residual Block*: This section compares the proposed GuidedNet with the same network using a general residual block (RB). We only replace the ERB structure with the general RB, retraining it on the same training dataset and with the same settings. Table V shows the average running

TABLE V

AVERAGE QIS WITH THE RELATED STANDARD DEVIATIONS OF THE RESULTS ON CAVE AND HARVARD DATASETS BY OUR METHOD USING THE TRADITIONAL RB AND THE PROPOSED ERB

CAVE					
Method	PSNR	SAM	ERGAS	SSIM	Time(s)
RB	45.05±3.6	3.93±1.3	0.980±0.7	0.992±0.00	0.37
ERB	45.41±3.6	4.03±1.3	0.969±0.7	0.991±0.00	0.26
Harvard					
Method	PSNR	SAM	ERGAS	SSIM	Time(s)
RB	37.45±7.4	5.04±2.7	12.7±28.8	0.953±0.05	0.72
ERB	37.96±6.8	4.48±2.0	3.52±2.5	0.961±0.03	0.50

times and QIs on 11 testing CAVE images and ten Harvard testing images. It is clear that the ERB can significantly reduce the computational burden and improve the performance.

3) *Multiscale Loss*: In this section, we investigate the role of the weights, α_k , in the loss function. We set some weights for the loss function, then retraining the network and obtaining the results on the CAVE dataset. A set of weights is tested on the same training set. We will use the following notation: (w_1, w_2, w_3) , where we have three layers with three different weights, that is, w_1 , w_2 , and w_3 . w_1 is related to the first (initial) layer, w_2 is about the second (intermediate) layer, and w_3 refers to the final layer. For instance, if the $\{\alpha_k\}_{k=1,\dots,3}$ are set to $(0, 0, 1)$, no initial and intermediate multiscale losses are considered in the loss function. The average QIs are in Table VI. We can note that when we have that $\{\alpha_k\}_{k=1,\dots,3} = (4, 2, 1)$, the proposed method produces the best results avoiding instability caused by too low or too high weights.

4) *PMS and DDS*: We modify the network to verify the validity of the FRB's PMS and the DDS. More specifically, the network uses only one DFM with a scaling factor of 8 and does not downsample multiscale MSIs to obtain a network

TABLE VI
AVERAGE QIS WITH THE RELATED STANDARD DEVIATIONS OF THE RESULTS ON THE CAVE DATASET USING DIFFERENT WEIGHTS CONFIGURATIONS. THE BEST RESULTS ARE HIGHLIGHTED

$\{\alpha_k\}_{k=1,\dots,3}$	PSNR	SAM	ERGAS	SSIM
(0, 0, 1)	44.55±8.9	3.97±1.2	1.06±0.8	0.991±0.00
(1, 2, 4)	43.55±4.5	3.96±1.1	1.25±1.2	0.990±0.01
(1, 1, 1)	45.09±3.7	3.82±1.2	0.984±0.7	0.991±0.00
(16, 4, 1)	44.93±3.5	4.31±1.5	1.01±0.7	0.990±0.00
(4, 2, 1)	45.41±3.6	4.03±1.3	0.969±0.7	0.991±0.00

TABLE VII
THE EFFECTS OF THE PMS AND THE DDS IN THE PROPOSED GUIDEDNET ON THE CAVE DATASET. THE BEST RESULTS ARE HIGHLIGHTED

Method	PSNR	SAM	ERGAS	SSIM
w/o PMS	43.57±4.9	4.43±1.3	1.38±1.2	0.989±0.01
w/o DDS	44.38±3.9	4.26±1.5	1.22±0.9	0.990±0.00
GuidedNet	45.41±3.6	4.03±1.3	0.97±0.7	0.991±0.00

TABLE VIII
AVERAGE QIS WITH THE RELATED STANDARD DEVIATIONS OF THE PROPOSED GUIDEDNET AND THE MHF-NET TRAINED ON THE CAVE TRAINING SET AND TESTED ON TEN TESTING IMAGES FROM THE HARVARD DATASET. THE BEST RESULTS ARE HIGHLIGHTED

Method	PSNR	SAM	ERGAS	SSIM
MHF-net [6]	37.24±7.5	6.21±3.9	17.27±39.84	0.943±0.06
HSRnet [37]	37.85±7.2	4.35±1.7	3.48±1.5	0.958±0.05
GuidedNet	37.96±6.8	4.48±2.0	3.52±2.5	0.961±0.03

without PMS (w/o PMS). Note that the GuidedNet (w/o PMS) requires an $8\times$ upsampling, and we expanded the final convolution kernel size to 7 to avoid significant degradation in performance. The DDS in the FRB is set to a single data stream by modifying the DFM to make the input and output only having one HSI. The experimental results using the same hyperparameters are shown in Table VII. The results in the table indicate that the performance significantly drops when we remove the PMS. Moreover, removing the DDS structure results in a performance reduction. The complete GuidedNet, holding both the structures, yields the best outcome demonstrating the importance of the PMS and the DDS structure in the proposed GuidedNet.

D. Comparison With DL-Based Methods

In this section, the two DL-based HISR methods are compared in more detail giving information about some aspects, such as network generalization and complexity.

1) *Network Generalization*: Network generalization is crucial to demonstrate the effectiveness of data-driven approaches. Thus, this section investigates the network generalization ability of the MHF-net, the HSRnet, and the GuidedNet. All the approaches are trained on the CAVE training set and then tested on the Harvard testing set. Table VIII reports the average QIs and standard deviations. The proposed method outperforms the other methods considering the PSNR and SSIM metrics, while HSRnet shows advantages referring to the SAM and ERGAS metrics.

TABLE IX
PARAMETER AMOUNT AND FLOPs PER SECOND OF THE GUIDEDNET, THE MHF-NET, AND THE HSRNET

Method	# Params.	FLOPs	Training time
MHF-net [6]	2.03M	53.27G	$14.9 \times 10^4 s$
HSRnet [37]	1.98M	45.33G	$2.6 \times 10^4 s$
GuidedNet (w/o PMS)	0.81M	34.68G	$2.2 \times 10^4 s$
GuidedNet (w/o DDS)	0.69M	32.79G	$2.1 \times 10^4 s$
GuidedNet	0.70M	35.31G	$2.1 \times 10^4 s$

TABLE X
AVERAGE QIS WITH THE RELATED STANDARD DEVIATIONS OF THE RESULTS PROVIDED BY THE ALL METHODS ON 11 TESTING IMAGES FROM THE CAVE DATASET WITH A SCALING FACTOR OF $4\times$. THE BEST RESULTS ARE HIGHLIGHTED

Method	PSNR	SAM	ERGAS	SSIM
CNMF [18]	41.59±2.9	8.10±3.4	3.99±3.2	0.972±0.02
FUSE [57]	39.71±3.5	5.83±2.0	4.19±3.1	0.975±0.02
GLP-HS [58]	37.81±3.1	5.36±1.8	4.66±2.7	0.972±0.01
LTTR [19]	36.76±2.8	6.60±2.5	5.65±2.8	0.957±0.03
LTMR [5]	36.19±2.7	7.66±2.8	5.70±2.7	0.949±0.03
IR-TenSR [59]	36.38±2.6	8.7±3.0	5.52±2.6	0.948±0.03
MHF-net [6]	46.27±2.7	4.33±1.8	1.74±1.2	0.992±0.00
HSRnet [37]	47.71±2.7	2.95±1.0	1.39±0.8	0.994±0.00
GuidedNet	47.64±3.2	3.29±1.2	1.47±1.0	0.994±0.00

2) *Network Complexity*: Table IX shows the network parameters number, the floating-point operations (FLOPs), and the training times of the three compared approaches. It is easily remarked that the GuidedNet has fewer parameters and computations with respect to the MHF-net and HSRnet. Furthermore, the GuidedNet takes less training time, and, as discussed earlier, the average testing times of the GuidedNet on both the CAVE and the Harvard datasets are shorter. Moreover, we also compare the hardware consumption and training times of the GuidedNet without PMS and DDS. From Table IX, it can be seen that PMS and DDS can improve performance without significantly increasing hardware consumption.

3) *Results on Different Scaling Factors*: By changing the number of recursive DFMs, the proposed GuidedNet can easily reach any super-resolution scaling factor power of 2. In the previous experiments, we tested the performance of HISR on a scaling factor equal to 8. This section investigates fusion performance varying the scaling factors (e.g., 4, 8, 16, and 32). Concerning the data simulation, we only need to change the scaling factor of the downsampling while keeping the other network settings unchanged. In Table X, we compare the performance of the used benchmark exploiting a scaling factor of 4 and measuring an average and the corresponding standard deviations for all the QIs. This table shows that the HSRnet obtains the best results on PSNR, SAM, and ERGAS, and our GuidedNet gets the best SSIM. All the traditional approaches show a significant gap comparing them with the two DL-based methods (i.e., the MHF-net and the HSRnet) and the GuidedNet.

Moreover, we also depicted the corresponding pseudo-color images of the HISR outputs in Fig. 10. We can see that the proposed GuidedNet obtains fewer residuals than the other approaches demonstrating its effectiveness. Finally, Table XI

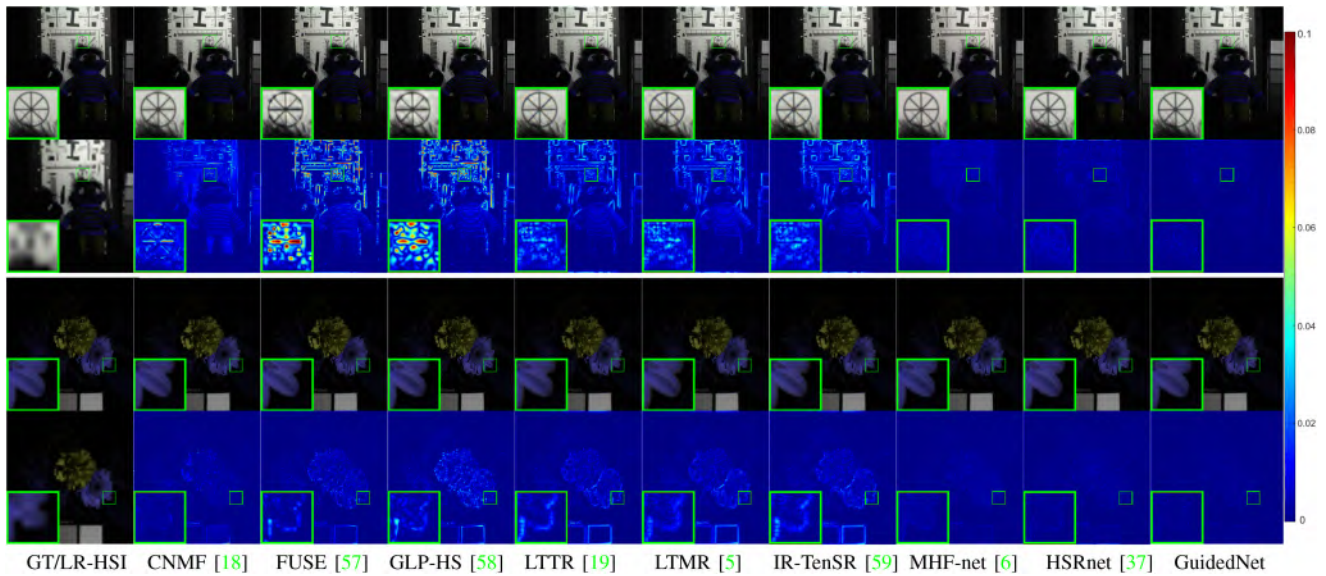


Fig. 10. HISR with a scaling factor $4\times$. The first column: the GTs and the corresponding LR-HSI images (in pseudo-colors) for the *chart* and *stuffed toy* (R-2, G-11, B-5) (1st and 2nd rows) and the *flowers* (R-27, G-21, B-26) (3rd and 4th rows) test cases from the CAVE dataset. The 2nd–8th columns: the visual results and the related error maps for all the compared approaches. A zoomed area has been added to aid the visual inspection.

TABLE XI
AVERAGE QIS WITH THE RELATED STANDARD DEVIATIONS OF THE RESULTS PROVIDED BY THE MHF-NET, THE HSRNET, AND THE GUIDEDNET FOR 11 TESTING IMAGES ON THE CAVE DATASET CONSIDERING AS SCALING FACTORS $16\times$ AND $32\times$

$16\times$				
Method	PSNR	SAM	ERGAS	SSIM
MHF-net [6]	43.33 \pm 3.5	5.58 \pm 1.9	0.627 \pm 0.45	0.987 \pm 0.01
HSRnet [37]	42.82 \pm 3.8	5.05 \pm 1.8	0.691 \pm 0.44	0.984 \pm 0.01
GuidedNet	43.39\pm3.9	4.70\pm1.5	0.605\pm0.47	0.989\pm0.01
$32\times$				
Method	PSNR	SAM	ERGAS	SSIM
MHF-net [6]	41.91 \pm 4.0	6.23\pm2.1	0.371 \pm 0.30	0.985\pm0.01
HSRnet [37]	39.64 \pm 2.8	6.85 \pm 2.4	0.507 \pm 0.34	0.969 \pm 0.02
GuidedNet	41.98\pm3.5	6.66 \pm 2.3	0.336\pm0.21	0.984 \pm 0.01

also reports the quantitative outcomes of the three DL-based methods on larger scaling factors, that is, 16 and 32. Some other traditional methods cannot achieve the task of $32\times$, or codes are not runnable on larger scale factors. Thus, we, here, only add a comparison with MHF-net and HSRnet since they can be run on larger scale factors and are also DL-based methods. From Table XI, it is clear that the GuidedNet approach shows competitive performance in these other configurations demonstrating a good adaptation for addressing diverse scale fusion problems. Compared to the scale factor of 4, the performance of HSRnet decreases significantly as the scale factor increases because of the used upsampling strategy.

E. Extension to Other Applications

As mentioned before, the GuidedNet is a general fusion framework that can effectively fuse an LR input with HR guidance to reach a higher resolution. Thanks to the proposed

general paradigm, we can extend the GuidedNet to other resolution enhancement tasks when there is an HR guidance. In what follows, we apply GuidedNet to two image resolution enhancement problems, that is, remote sensing pansharpening and SISR.

1) *Pansharpening*: Pansharpening is about fusing a low-resolution multispectral image (LR-MSI) and a PAN image with high spatial resolution, aiming to obtain an HR-MSI with the exact spatial resolution as the PAN image. More details about pansharpening can be found in a recent review [66]. The pansharpening task shares some similarities with the MSI/HSI fusion task. Therefore, following the MSI/HSI fusion framework of the GuidedNet, we only need to replace the HR-MSI in Fig. 2 with the PAN image and substitute the LR-HSI in Fig. 2 with the LR-MSI. It is worth noting that the scaling factor for pansharpening is often 4 (at least for the primary adopted sensors). Thus, we reduced the number of recursive DFMs to 2. We employed an 8-band multispectral dataset acquired by the WorldView-3 (WV-3) sensor for the training. The process of building training and testing data is described in [52]. Thus, we have 8806 PAN (64×64), LR-MSI ($16 \times 16 \times 8$), and HR-MSI ($64 \times 64 \times 8$) image patch pairs as the training set. For the sake of brevity, we do not introduce details about the data used. Readers can refer to [52] and [67] for more information. Moreover, the quality of the fusion results is evaluated using the SAM [63], the ERGAS [64], the spatial correlation coefficient (SCC) [68], and the universal image quality index for eight-band images (Q8) [69].

For this application, we compare our approach with four SOTA DL-based pansharpening methods, that is, PNN [48], PanNet [47], DMDnet [49], and FusionNet [52]. Table XII reports the outcomes for all the compared approaches on 1258 randomly selected training samples. From the average QIs and the related standard deviations shown in Table XII,

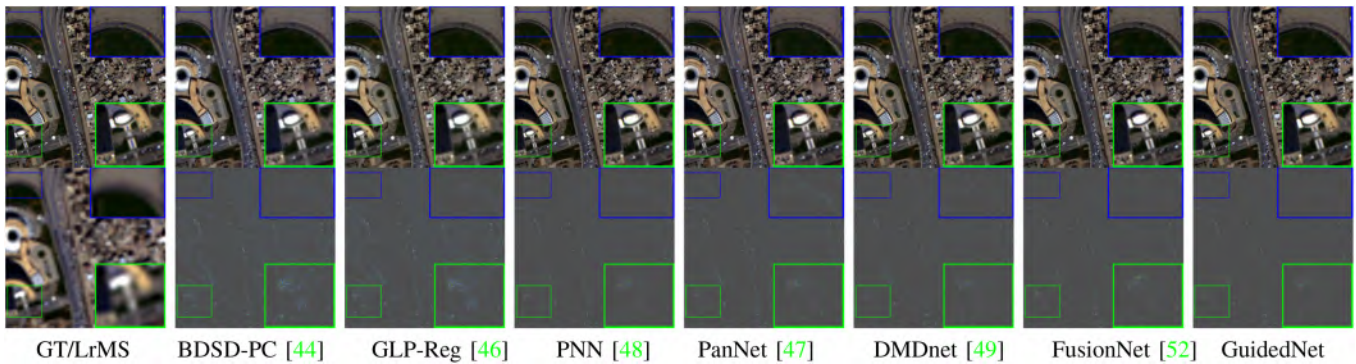


Fig. 11. Visual comparison of pansharpening products on the *Rio* datasets acquired by the WV-3 sensor. Two zoomed areas have been added to aid the visual inspection.

TABLE XII

AVERAGE QIS WITH THE RELATED STANDARD DEVIATIONS OF THE PANSHARPENING RESULTS PROVIDED BY DIFFERENT METHODS FOR 1258 TESTING IMAGES ON THE WV-3 DATASET. THE BEST VALUES ARE HIGHLIGHTED IN BOLDFACE

Method	SAM	ERGAS	SCC	Q8
PNN [48]	4.00±1.3	2.72±1.0	0.962±0.05	0.908±0.11
PanNet [47]	4.09±1.3	2.95±1.0	0.949±0.05	0.894±0.11
DMDnet [49]	3.97±1.2	2.86±1.0	0.953±0.04	0.900±0.11
FusionNet [52]	3.74±1.2	2.57±0.9	0.958±0.05	0.914±0.11
GuidedNet	3.50±1.2	2.39±0.9	0.963±0.04	0.922±0.10

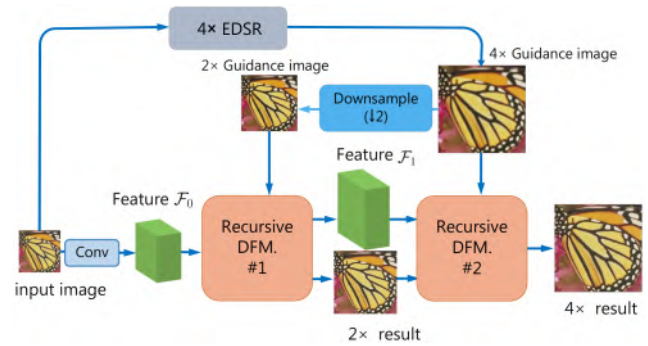


Fig. 12. Extended architecture of the GuidedNet for the 4× SISR task. EDSR has been pretrained and its results are directly used as input.

it is clear that the GuidedNet yields the best quantitative performance on all the indicators, that is, SAM, ERGAS, SCC, and Q8. Besides, for qualitative comparison, we augment the benchmark even including a CS-based approach, that is, the BSDS-PC, and an MRA-based method, that is, the GLP-Reg. Fig. 11 depicts the results on WV-3, indicating that the image reconstructed by the proposed method is more precise than the comparison methods. The GuidedNet’s satisfactory results on pansharpening demonstrate its ability to address different tasks.

2) *Single-Image Super-Resolution*: The GuidedNet fusion framework can also be extended to the SISR problem. However, the proposed fusion framework requires high-resolution guidance to enhance the resolution. Instead, the SISR has a unique input, the LR image. Therefore, we need to introduce high-resolution guidance into the framework. Here, we use the outcome of a competitive SISR method, that is, the DL-based SISR approach EDSR [40], to replace the HR-MSI in the HGB in Fig. 2. Fig. 12 depicts the GuidedNet structure for the 4× SISR task modified by the addition of EDSR. EDSR has been pretrained using the DIV2K dataset by the Adam optimizer, and we only utilize its testing outcomes as input in the HGB branch of our GuidedNet. It is not necessary to retrain the EDSR again in GuidedNet. The training parameters are the default ones in [40], that is, the batch size is set to 16, and the learning rate is initialized to 0.0001 halved at every 1×10^6 batch updates. The scaling factor is 4. Thus, the GuidedNet for SISR requires two recursive DFMs. The proposed approach is again trained using the DIV2K dataset [70].

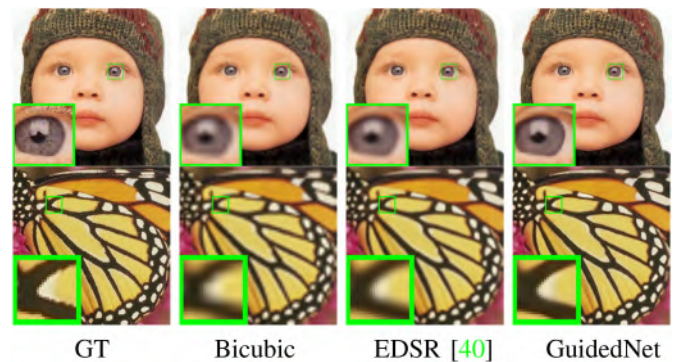


Fig. 13. Results provided by the benchmark with a scaling factor of 4 for the *baby* and the *butterfly* test cases from the Set5 dataset. A zoomed area has been added to aid the visual inspection.

After ending the training of the GuidedNet, the trained network is evaluated on the Set5 testing dataset. Table XIII reports the average PSNR and SSIM values of the bicubic interpolation, the SOTA EDSR, and the GuidedNet. The proposed method can significantly improve the results of EDSR, even outperforming the classical bicubic interpolator. By looking at the visual comparison shown in Fig. 13, the GuidedNet approach holds sharper details, especially, comparing them with the ones of the baseline method, EDSR. In this case, we consider the outcome of the EDSR method into the HGB (viewed as a plug-in module). However, we can take

TABLE XIII
QIS OF THE RESULTS PROVIDED BY THE BENCHMARK ON THE SET5
DATASET FOR SISR WITH SCALING FACTOR OF 4×

Set5			
Method	bicubic PSNR/SSIM	EDSR [40] PSNR/SSIM	GuidedNet PSNR/SSIM
<i>baby</i>	31.83/0.858	32.54/0.869	33.64/0.892
<i>bird</i>	30.05/0.870	31.34/0.898	34.00/0.934
<i>butterfly</i>	22.15/0.734	23.54/0.801	27.30/0.901
<i>head</i>	32.67/0.754	32.70/0.764	32.91/0.794
<i>woman</i>	26.44/0.831	27.56/0.861	30.02/0.907
average	28.43/0.810	29.54/0.839	31.57/0.886

any baseline SISR method into our GuidedNet framework to enhance the SR performance.

V. CONCLUSION

This article proposed a general CNN fusion framework, GuidedNet, to deal with the HISR problem thanks to high-resolution guidance. Motivated by the specific problem (i.e., the HISR), this framework has been formulated using two branches: 1) the HGB and 2) the FRB. Besides, by considering some strategies, such as the recursive mechanism and the progressive technique, the proposed GuidedNet can significantly reduce the network parameters getting high-quality outcomes. Extensive experiments on several HSI datasets demonstrate the superiority of the proposed GuidedNet, comparing it with recent SOTA approaches. Furthermore, discussions about several aspects, such as network generalization, network complexity, robustness with respect to variations of scaling factors, and time comparison, have been provided to the readers. Finally, the proposed fusion framework has been easily extended to other resolution enhancement tasks, that is, remote sensing pansharpening and SISR.

REFERENCES

- [1] J. M. Bioucas-Dias, A. Plaza, G. Camps-Valls, P. Scheunders, N. Nasrabadi, and J. Chanussot, "Hyperspectral remote sensing data analysis and future challenges," *IEEE Trans. Geosci. Remote Sens.*, vol. 1, no. 2, pp. 6–36, Jun. 2013.
- [2] M. Bergeron et al., "Hyperspectral environment and resource observer (HERO) mission," *Can. J. Remote Sens.*, vol. 34, no. suppl, pp. S1–S11, 2008.
- [3] H. Yuan and Y. Y. Tang, "Spectral-spatial shared linear regression for hyperspectral image classification," *IEEE Trans. Cybern.*, vol. 47, no. 4, pp. 934–945, Apr. 2017.
- [4] M. Uzair, A. Mahmood, and A. Mian, "Hyperspectral face recognition using 3D-DCT and partial least squares," in *Proc. Brit. Mach. Vis. Conf. (BMVC)*, 2013, pp. 1–9.
- [5] R. Dian and S. Li, "Hyperspectral image super-resolution via subspace-based low tensor multi-rank regularization," *IEEE Trans. Image Process.*, vol. 28, no. 10, pp. 5135–5146, Oct. 2019.
- [6] Q. Xie, M. Zhou, Q. Zhao, Z. Xu, and D. Meng, "MHF-net: An interpretable deep network for multispectral and hyperspectral image fusion," *IEEE Trans. Pattern Anal. Mach. Intell.*, vol. 44, no. 3, pp. 1457–1473, Mar. 2022.
- [7] T.-X. Jiang, T.-Z. Huang, X.-L. Zhao, L.-J. Deng, and Y. Wang, "A novel tensor-based video rain streaks removal approach via Utilizing discriminatively intrinsic priors," in *Proc. IEEE Conf. Comput. Vis. Pattern Recognit. (CVPR)*, 2017, pp. 2818–2827.
- [8] J. Jiang, J. Ma, C. Chen, X. Jiang, and Z. Wang, "Noise robust face image super-resolution through smooth sparse representation," *IEEE Trans. Cybern.*, vol. 47, no. 11, pp. 3991–4002, Nov. 2017.
- [9] T.-X. Jiang, T.-Z. Huang, X.-L. Zhao, L.-J. Deng, and Y. Wang, "FastDeRain: A novel video rain streak removal method using directional gradient priors," *IEEE Trans. Image Process.*, vol. 28, no. 4, pp. 2089–2102, Apr. 2019.
- [10] L.-J. Deng, W. Guo, and T.-Z. Huang, "Single-image super-resolution via an iterative reproducing kernel Hilbert space method," *IEEE Trans. Circuit Syst. Video Technol.*, vol. 26, no. 11, pp. 2001–2014, Nov. 2016.
- [11] Y. Chang, L. Yan, X.-L. Zhao, H. Fang, Z. Zhang, and S. Zhong, "Weighted low-rank tensor recovery for hyperspectral image restoration," *IEEE Trans. Cybern.*, vol. 50, no. 11, pp. 4558–4572, Nov. 2020.
- [12] L.-J. Deng, G. Vivone, W. Guo, M. D. Mura, and J. Chanussot, "A variational pansharpening approach based on reproducible kernel Hilbert space and heaviside function," *IEEE Trans. Image Process.*, vol. 27, no. 9, pp. 4330–4344, Sep. 2018.
- [13] Z.-C. Wu et al., "A new variational approach based on proximal deep injection and gradient intensity similarity for spatio-spectral image fusion," *IEEE J. Sel. Topics Appl. Earth Observ. Remote Sens.*, vol. 13, pp. 6277–6290, 2020.
- [14] P. Guo, P. Zhuang, and Y. Guo, "Bayesian pan-sharpening with multi-order gradient-based deep network constraints," *IEEE J. Sel. Topics Appl. Earth Observ. Remote Sens.*, vol. 13, pp. 950–962, 2020.
- [15] P. Zhuang, Q. Liu, and X. Ding, "Pan-GGF: A probabilistic method for pan-sharpening with gradient domain guided image filtering," *Signal Process.*, vol. 156, pp. 177–190, Mar. 2019.
- [16] R. Dian, S. Li, L. Fang, T. Lu, and J. M. Bioucas-Dias, "Nonlocal sparse tensor factorization for semiblind hyperspectral and multispectral image fusion," *IEEE Trans. Cybern.*, vol. 50, no. 10, pp. 4469–4480, Oct. 2020.
- [17] Z. H. Nezhad, A. Karami, R. Heylen, and P. Scheunders, "Fusion of hyperspectral and multispectral images using spectral unmixing and sparse coding," *IEEE J. Sel. Topics Appl. Earth Observ. Remote Sens.*, vol. 9, no. 6, pp. 2377–2389, Jun. 2016.
- [18] N. Yokoya, T. Yairi, and A. Iwasaki, "Coupled nonnegative matrix factorization unmixing for hyperspectral and multispectral data fusion," *IEEE Trans. Geosci. Remote Sens.*, vol. 50, no. 2, pp. 528–537, Feb. 2012.
- [19] R. Dian, S. Li, and L. Fang, "Learning a low tensor-train rank representation for hyperspectral image super-resolution," *IEEE Trans. Neural Netw. Learn. Syst.*, vol. 30, no. 9, pp. 2672–2683, Sep. 2019.
- [20] R. A. Borsoi, T. Imbiriba, and J. C. M. Bermudez, "Super-resolution for hyperspectral and multispectral image fusion accounting for seasonal spectral variability," *IEEE Trans. Image Process.*, vol. 29, pp. 116–127, 2020.
- [21] R. Dian, S. Li, and X. Kang, "Regularizing hyperspectral and multispectral image fusion by CNN denoiser," *IEEE Trans. Neural Netw. Learn. Syst.*, vol. 32, no. 3, pp. 1124–1135, Mar. 2021.
- [22] T. Xu, T.-Z. Huang, L.-J. Deng, X.-L. Zhao, and J. Huang, "Hyperspectral image Superresolution using unidirectional total variation with tucker decomposition," *IEEE J. Sel. Topics Appl. Earth Observ. Remote Sens.*, vol. 13, pp. 4381–4398, 2020.
- [23] W.-S. Lai, J.-B. Huang, N. Ahuja, and M.-H. Yang, "Fast and accurate image super-resolution with deep Laplacian pyramid networks," *IEEE Trans. Pattern Anal. Mach. Intell.*, vol. 41, no. 11, pp. 2599–2613, Nov. 2019.
- [24] R. Lan et al., "Cascading and enhanced residual networks for accurate single-image super-resolution," *IEEE Trans. Cybern.*, vol. 51, no. 1, pp. 115–125, Jan. 2021.
- [25] Y. Zhou, X. Du, M. Wang, S. Huo, Y. Zhang, and S.-Y. Kung, "Cross-scale residual network: A general framework for image super-resolution, denoising, and deblocking," *IEEE Trans. Cybern.*, vol. 52, no. 7, pp. 5855–5867, Jul. 2022.
- [26] C. Ren, X. He, Y. Pu, and T. Q. Nguyen, "Learning image profile enhancement and denoising statistics priors for single-image super-resolution," *IEEE Trans. Cybern.*, vol. 51, no. 7, pp. 3535–3548, Jul. 2021.
- [27] X. Liu, L. Li, F. Liu, B. Hou, S. Yang, and L. Jiao, "GAFnet: Group attention fusion network for PAN and MS image high-resolution classification," *IEEE Trans. Cybern.*, vol. 52, no. 10, pp. 10556–10569, Oct. 2022.
- [28] Z. Yu, J. Yu, C. Xiang, J. Fan, and D. Tao, "Beyond bilinear: Generalized multimodal factorized high-order pooling for visual question answering," *IEEE Trans. Neural Netw. Learn. Syst.*, vol. 29, no. 12, pp. 5947–5959, Dec. 2018.
- [29] R. Dian, S. Li, A. Guo, and L. Fang, "Deep hyperspectral image sharpening," *IEEE Trans. Neural Netw. Learn. Syst.*, vol. 29, no. 11, pp. 5345–5355, Nov. 2018.

- [30] F. Palsson, J. R. Sveinsson, and M. O. Ulfarsson, "Multispectral and hyperspectral image fusion using a 3-D-convolutional neural network," *IEEE Geosci. Remote Sens. Lett.*, vol. 14, no. 5, pp. 639–643, May 2017.
- [31] Q. Xie, M. Zhou, Q. Zhao, D. Meng, W. Zuo, and Z. Xu, "Multispectral and hyperspectral image fusion by MS/HS fusion net," in *Proc. IEEE Conf. Comput. Vis. Pattern Recognit. (CVPR)*, 2019, pp. 1585–1594.
- [32] X.-H. Han, Y. Zheng, and Y.-W. Chen, "Multi-level and multi-scale spatial and spectral fusion CNN for hyperspectral image super-resolution," in *Proc. Int. Conf. Comput. Vis. Workshop (ICCVW)*, 2019, pp. 4330–4339.
- [33] Z. Zhu, J. Hou, J. Chen, H. Zeng, and J. Zhou, "Hyperspectral image super-resolution via deep progressive zero-centric residual learning," *IEEE Trans. Image Process.*, vol. 30, pp. 1423–1438, 2020.
- [34] F. Zhou, R. Hang, Q. Liu, and X. Yuan, "Pyramid fully convolutional network for hyperspectral and multispectral image fusion," *IEEE J. Sel. Topics Appl. Earth Observ. Remote Sens.*, vol. 12, no. 5, pp. 1549–1558, May 2019.
- [35] S. Xu, O. Amira, J. Liu, C.-X. Zhang, J. Zhang, and G. Li, "HAM-MFN: Hyperspectral and multispectral image multiscale fusion network with RAP loss," *IEEE Trans. Geosci. Remote Sens.*, vol. 58, no. 7, pp. 4618–4628, Jul. 2020.
- [36] K. Zheng et al., "Coupled convolutional neural network with adaptive response function learning for unsupervised hyperspectral super resolution," *IEEE Trans. Geosci. Remote Sens.*, vol. 59, no. 3, pp. 2487–2502, Mar. 2021.
- [37] J.-F. Hu, T.-Z. Huang, L.-J. Deng, T.-X. Jiang, G. Vivone, and J. Chanussot, "Hyperspectral image super-resolution via deep spatio-spectral attention convolutional neural networks," *IEEE Trans. Neural Netw. Learn. Syst.*, vol. 33, no. 12, pp. 7251–7265, Dec. 2022.
- [38] G. Vivone, "Multispectral and hyperspectral image fusion in remote sensing: A survey," *Inf. Fusion*, vol. 89, pp. 405–417, Jan. 2023.
- [39] C. I. Kanatsoulis, X. Fu, N. D. Sidiropoulos, and W.-K. Ma, "Hyperspectral super-resolution via coupled tensor factorization: Identifiability and algorithms," in *Proc. IEEE Int. Conf. Acoust. Speech Signal. Process. (ICASSP)*, 2018, pp. 3191–3195.
- [40] B. Lim, S. Son, H. Kim, S. Nah, and K. Mu Lee, "Enhanced deep residual networks for single image super-resolution," in *Proc. IEEE Conf. Comput. Vis. Pattern Recognit. Workshop (CVPRW)*, 2017, pp. 136–144.
- [41] K. Zeng, J. Yu, R. Wang, C. Li, and D. Tao, "Coupled deep autoencoder for single image super-resolution," *IEEE Trans. Cybern.*, vol. 47, no. 1, pp. 27–37, Jan. 2017.
- [42] T. Wang, F. Fang, H. Zheng, and G. Zhang, "FrMLNet: Framelet-based multilevel network for Pansharpening," *IEEE Trans. Cybern.*, early access, Dec. 15, 2021, doi: [10.1109/TCYB.2021.3131651](https://doi.org/10.1109/TCYB.2021.3131651).
- [43] A. Garzelli, F. Nencini, and L. Capobianco, "Optimal MMSE pan sharpening of very high resolution multispectral images," *IEEE Trans. Geosci. Remote Sens.*, vol. 46, no. 1, pp. 228–236, Jan. 2008.
- [44] G. Vivone, "Robust band-dependent spatial-detail approaches for panchromatic sharpening," *IEEE Trans. Geosci. Remote Sens.*, vol. 57, no. 9, pp. 6421–6433, Sep. 2019.
- [45] B. Aiazzi, L. Alparone, S. Baronti, and A. Garzelli, "Context-driven fusion of high spatial and spectral resolution images based on over-sampled multiresolution analysis," *IEEE Trans. Geosci. Remote Sens.*, vol. 40, no. 10, pp. 2300–2312, Oct. 2002.
- [46] G. Vivone, R. Restaino, and J. Chanussot, "Full scale regression-based injection coefficients for panchromatic sharpening," *IEEE Trans. Image Process.*, vol. 27, no. 7, pp. 3418–3431, Jul. 2018.
- [47] J. Yang, X. Fu, Y. Hu, Y. Huang, X. Ding, and J. Paisley, "PanNet: A deep network architecture for pan-sharpening," in *Proc. Int. Conf. Comput. Vis. (ICCV)*, 2017, pp. 5449–5457.
- [48] G. Masi, D. Cozzolino, L. Verdoliva, and G. Scarpa, "Pansharpening by convolutional neural networks," *Remote Sens.*, vol. 8, no. 7, p. 594, 2016.
- [49] X. Fu, W. Wang, Y. Huang, X. Ding, and J. Paisley, "Deep multiscale detail networks for multiband spectral image sharpening," *IEEE Trans. Neural Netw. Learn. Syst.*, vol. 32, no. 5, pp. 2090–2104, May 2021.
- [50] L. He et al., "Pansharpening via detail injection based convolutional neural networks," *IEEE J. Sel. Topics Appl. Earth Observ. Remote Sens.*, vol. 12, no. 4, pp. 1188–1204, Apr. 2019.
- [51] Y. Wei, Q. Yuan, H. Shen, and L. Zhang, "Boosting the accuracy of multispectral image pansharpening by learning a deep residual network," *IEEE Geosci. Remote Sens. Lett.*, vol. 14, no. 10, pp. 1795–1799, Mar. 2017.
- [52] L.-J. Deng, G. Vivone, C. Jin, and J. Chanussot, "Detail injection-based deep convolutional neural networks for pansharpening," *IEEE Trans. Geosci. Remote Sens.*, vol. 59, no. 8, pp. 6995–7010, Aug. 2021.
- [53] Z.-C. Wu, T.-Z. Huang, L.-J. Deng, J.-F. Hu, and G. Vivone, "VO+net: An adaptive approach using variational optimization and deep learning for panchromatic sharpening," *IEEE Trans. Geosci. Remote Sens.*, vol. 60, 2021, Art. no. 5401016.
- [54] Y. Zhang, C. Liu, M. Sun, and Y. Ou, "Pan-sharpening using an efficient bidirectional pyramid network," *IEEE Trans. Geosci. Remote Sens.*, vol. 57, no. 8, pp. 5549–5563, Aug. 2019.
- [55] T.-W. Hui, C. C. Loy, and X. Tang, "Depth map super-resolution by deep multi-scale guidance," in *Proc. Eur. Conf. Comput. Vis. (ECCV)*, 2016, pp. 353–369.
- [56] G. Huang, Z. Liu, L. Van Der Maaten, and K. Q. Weinberger, "Densely connected convolutional networks," in *Proc. IEEE Conf. Comput. Vis. Pattern Recognit. (CVPR)*, 2017, pp. 4700–4708.
- [57] Q. Wei, N. Dobigeon, and J.-Y. Tourneret, "Fast fusion of multi-band images based on solving a Sylvester equation," *IEEE Trans. Image Process.*, vol. 24, no. 11, pp. 4109–4121, Nov. 2015.
- [58] M. Selva, B. Aiazzi, F. Butera, L. Chiarantini, and S. Baronti, "Hyper-sharpening: A first approach on SIM-GA data," *IEEE J. Sel. Topics Appl. Earth Observ. Remote Sens.*, vol. 8, no. 6, pp. 3008–3024, Jun. 2015.
- [59] T. Xu, T.-Z. Huang, L.-J. Deng, and N. Yokoya, "An iterative regularization method based on tensor subspace representation for hyperspectral image super-resolution," *IEEE Trans. Geosci. Remote Sens.*, vol. 60, pp. 1–16, 2022.
- [60] F. Yasuma, T. Mitsunaga, D. Iso, and S. K. Nayar, "Generalized assorted pixel camera: Postcapture control of resolution, dynamic range, and spectrum," *IEEE Trans. Image Process.*, vol. 19, no. 9, p. 2241, Sep. 2010.
- [61] A. Chakrabarti and T. Zickler, "Statistics of real-world hyperspectral images," in *Proc. IEEE Conf. Comput. Vis. Pattern Recognit. (CVPR)*, 2011, pp. 193–200.
- [62] D. Kingma and J. Ba, "Adam: A method for stochastic optimization," in *Proc. Int. Conf. Learn. Rep. (ICLR)*, Dec. 2014, pp. 1–6.
- [63] R. H. Yuhas, A. F. Goetz, and J. W. Boardman, "Discrimination among semi-arid landscape endmembers using the spectral angle mapper (SAM) algorithm," in *Proc. JPL Airborne Geosci. Workshop*, vol. 1, 1992, pp. 147–149.
- [64] L. Wald, *Data Fusion. Definitions and Architectures—Fusion of Images of Different Spatial Resolutions*, PSL Res. Univ., New York, NY, USA, 2002.
- [65] Z. Wang, A. C. Bovik, H. R. Sheikh, and E. P. Simoncelli, "Image quality assessment: From error visibility to structural similarity," *IEEE Trans. Image Process.*, vol. 13, no. 4, pp. 600–612, Apr. 2004.
- [66] G. Vivone et al., "A new benchmark based on recent advances in multispectral pansharpening: Revisiting pansharpening with classical and emerging pansharpening methods," *IEEE Geosci. Remote Sens. Mag.*, vol. 9, no. 1, pp. 53–81, Mar. 2021.
- [67] L.-J. Deng et al., "Machine learning in pansharpening: A benchmark, from shallow to deep networks," *IEEE Geosci. Remote Sens. Mag.*, vol. 10, no. 3, pp. 279–315, Sep. 2022.
- [68] J. Zhou, D. L. Civco, and J. A. Silander, "A wavelet transform method to merge landsat TM and SPOT panchromatic data," *Int. J. Remote Sens.*, vol. 19, no. 4, pp. 743–757, 1998.
- [69] A. Garzelli and F. Nencini, "Hypercomplex quality assessment of multi/hyperspectral images," *IEEE Geosci. Remote Sens. Lett.*, vol. 6, no. 4, pp. 662–665, Oct. 2009.
- [70] E. Agustsson and R. Timofte, "NTIRE 2017 challenge on single image super-resolution: Dataset and study," in *Proc. IEEE Conf. Comput. Vis. Pattern Recognit. Workshop (CVPRW)*, Jul. 2017, pp. 1122–1131.